

Capturing the colloidal microplastics with plant-based nanocellulose networks

Ilona Leppänen

VTT Technical Research Centre of Finland

Timo Lappalainen

VTT Technical Research Centre of Finland Ltd

Tiia Lohtander

Aalto University

Christopher Jonkergouw

Aalto University

Suvi Arola

VTT Technical Research Centre of Finland

Tekla Tammelin (✉ tekla.tammelin@vtt.fi)

VTT Technical Research Centre of Finland Ltd

Article

Keywords: colloidal microplastics, nanocellulose, recovery techniques, entrapment of particles

Posted Date: April 13th, 2021

DOI: <https://doi.org/10.21203/rs.3.rs-286541/v1>

License:  This work is licensed under a Creative Commons Attribution 4.0 International License.

[Read Full License](#)

Version of Record: A version of this preprint was published at Nature Communications on April 5th, 2022.
See the published version at <https://doi.org/10.1038/s41467-022-29446-7>.

1
2
3
4
5
6
7
8
9
10
11
12
13
14
15
16
17
18
19
20
21
22
23

Capturing the colloidal microplastics with plant-based nanocellulose networks

Author list

Ilona Leppänen¹, Timo Lappalainen¹, Tia Lohtander^{1,2}, Christopher Jonkergouw³, Suvi Arola^{1*} and
Tekla Tammelin^{1*}

¹ Biomass processing and products, VTT Technical Research Centre of Finland Ltd., FI-02044,
Espoo Finland

² Department of Bioproducts and Biosystems, School of Chemical Engineering, Aalto University,
Vuorimiehentie 1, 02150 Espoo, Finland.

³ Department of Bioproducts and Biosystems, School of Chemical Engineering, Aalto University,
Kemistintie 1, 02150 Espoo, Finland.

Abstract

Microplastics accumulate to various aquatic organisms causing serious health issues, and they have raised concerns about human health by entering our food chain. The recovery techniques for the most challenging colloidal fraction even for the analytical purposes are limited. Here we show how hygroscopic nanocellulose network acts as an ideal capturing material even for the tiniest nanoplastic particles. We reveal that the entrapment of particles from the aqueous environment is a result of the network's hygroscopic nature - a feature which is further intensified with the high surface area. We determine the nanoplastic binding mechanisms using surface sensitive methods, and interpret the results with the random sequential adsorption (RSA) model. The microplastic uptake does not rely on any specific interfacial interaction but rather on the water transport behavior of nanocellulose. These findings hold potential for the explicit quantification of the microplastics

24 from different environments, and eventually, provide solutions to collect those directly on-site
25 where they are produced.

26 Plastic pollution entering our environment at an increasing rate is a major problem, especially in the
27 marine environment¹⁻³. It is estimated that 8.8 million tons of plastic waste end up in oceans every
28 year⁴. Primary micro- (μ Pp, size $1\mu\text{m} - 5\text{mm}$) and nanoplastic (nPp, size $<1\mu\text{m}$) particles used in
29 i.e. pharmaceuticals and cosmetics can enter the environment directly. Erosion of plastics causes
30 fragmentation into smaller particles, namely secondary micro- and nanoplastic particles.^{5,6}
31 Nanoplastics are especially harmful due to their small size (hard to capture, can enter cells), large
32 surface area (capable to bind e.g. toxins), and colloidal nature (limited means for quantification and
33 qualification).⁵ A few studies have analysed their presence in aquatic animals such as fish and
34 molluscs where they have been found and quantified proving their existence.⁷ A recent study has
35 also shown their presence in human placenta⁸. Model nPp accumulate on algal cell surfaces⁹, to
36 various organs in mussels¹⁰, and to juvenile zebra fish^{11,12} affecting their quality of life. An
37 extensive amount of knowledge on the abundance of microplastic particles in different
38 environments is available¹³. Recent efforts to overcome the plastic challenge highlight how
39 genetically engineered enzymes can degrade plastics.¹⁴ This approach could also be a tool for
40 microplastic management. However, very little is known about the existence of nanoplastic particles
41 mainly due to the technical challenges associated with their capture, separation, and analysis¹⁵⁻¹⁷.
42 To date, there is no means to recover nPp from environmental samples for explicit quantification or
43 for the qualitative analysis since existing methods are based on different filtration and elutriation
44 techniques appropriate only for the larger-sized μ Pp ($>50\mu\text{m}$)^{6,18,19}. At best, particle diameters
45 varying from few microns up to tens of microns can be extracted via density flotation and methods
46 which are based on migration velocity differences²⁰. These restrictions leave a blind spot for the
47 recovery, quantification, and qualification of colloidal plastic particles ($\varnothing < 1\mu\text{m}$)¹⁶. Here we show
48 that lignocellulose-based networks can be harnessed to qualify and quantify even the most

49 challenging fraction of the colloidal plastics. Plant-sourced cellulose nanofibrils (CNF) are colloidal
50 level objects with lateral dimensions of 3-10 nm and length up to micrometers. Their water-
51 responsive nature, self-assembly, and other unique properties have only recently unraveled.²¹ More
52 specifically, they can effectively recover e.g. gold ions from waste waters²² and interact with
53 nanoparticles in general²¹. In the realm of nanoscaled materials, besides hydrophilicity and
54 abundance in nature, the assemblies are highly hygroscopic. Strong interactions with water
55 distinguish nanocelluloses from many other nanomaterials with similar properties in terms of large
56 surface area and high aspect ratio.²³

57 We evidence the capturing ability of nanocellulose networks by following the fluorescent intensity
58 of microplastic particles either in microfluidistic set-up or by simply using nanocellulose films as
59 elements to collect the particles from the aqueous dispersions. We utilized model polystyrene (PS)
60 particles with different surface charge and size, i.e. anionic and cationic μ Pp ($\phi = 1.0/1.1\mu\text{m}$) and
61 anionic and cationic nPp ($\phi = 100\text{nm}$) (Supplementary Table 1) to reveal the essential mechanisms
62 facilitating the capturing efficiency. We introduce an interfacial approach where particle adsorption
63 data is coupled with the sequential adsorption model, and hence, we are able to quantify the particle
64 uptake with kinetic information and provide a methodology for nanoparticle detection. Therefore,
65 with our approach, we tackle the critical challenges related to reliable microplastic quantification,
66 and we put forward the solutions for microplastic management where e.g. nanocellulose-based filter
67 systems are capable to capture plastic particles on-site before entering the environment.

68 **Nanocellulose hydrogels trap microplastic particles**

69 We followed the microplastics capturing capacity of native CNF hydrogels²⁴ in real-time using
70 microfluidistic analysis coupled with fluorescent imaging (Fig. 1a-b), a straightforward and semi-
71 quantitative concept to evidence the ability of nanocellulose hydrogel to trap polystyrene (PS) nano-
72 and microplastic particles (cationic/anionic nPp and μ Pp). The fluorescence intensity increased in
73 the microfluidic traps containing CNF with each cycle of particles of both size classes (Fig. 1c, d,

74 Supplementary Fig. 1, Extended Data Video 1 for positively charged particles, Supplementary Fig.
75 2 for negatively charged particles). Accumulation of the fluorescence intensity over time was as
76 much as 70% higher for the positively charged nPp system when compared to μ Pp system (Fig. 1c,
77 d). Also, the same applied to the negatively charged particles, however, the overall fluorescence
78 accumulation of negatively charged particles (Supplementary Fig. 2 and 3) was lower compared to
79 positively charged particles (Fig. 1c, d, Supplementary Fig. 3) and the difference between
80 negatively charged nPp and μ Pp accumulation was not as large as with the positively charged
81 particles. By analyzing the profile of the accumulated fluorescence within the CNF hydrogel
82 (Supplementary Fig. 3a) we saw that the nPp were able to penetrate the hydrogel deeper compared
83 to μ Pp, indicating that the hydrogel network is porous at the nanometer to micrometer scale
84 (Supplementary Fig. 3b). The charges seems not to play a great role in penetration into the hydrogel
85 network but seems to affect the quantity of captured particles (Supplementary Fig. 3b). Generally,
86 the fluorescence intensity of single microplastic particle is significantly higher than that of
87 nanoplastic particle, and thus, our results indicate that CNF hydrogel has a considerably higher
88 capability to capture nPp than μ Pp.

89 Hygroscopic nanocellulosic assemblies display peculiar water transport properties involving
90 capillary action and diffusion²³. With the aid of water flux, the smallest microplastics seem to be
91 conveyed inside the CNF hydrogel network. Moreover, the large surface area of the porous network
92 enhances cohesion facilitating the entrapment of microplastics.²⁵ The negative overall charge of
93 CNF also promotes the accumulation of positively charged particles, however, it does not prevent
94 the accumulation of negatively charged particles.

95 **Capturing of micro- and nanoplastics with nanocellulose films**

96 We assessed the ability of nanocellulose films to collect nPp and μ Pp using fluorescence
97 spectroscopy. This method allows the direct quantification of the number of microplastics from the
98 aqueous dispersion before and after immersion of the films (Supplementary Fig. 4). By using

99 particles with either anionic or cationic charge, we are able to further elucidate the capturing
100 mechanisms, i.e. whether the electrostatic interactions play a role along with the nanocellulose
101 network hygroscopicity. We used native CNF²⁴ and TEMPO-oxidized CNF²⁶ (Supplementary Fig.
102 5) - the grades with altered water responding tendency due to the phenomenon called
103 hornification²⁷. Due to the low anionic charge of native CNF (0.04 mmol g⁻¹) it tends to lose its
104 active surface area upon drying whereas the charge of TEMPO-CNF is remarkably higher (1.3
105 mmol g⁻¹) preventing the hornification and, therefore, the water responsive nature is retained.

106 The number of captured nPp and μ Pp per unit area of nanocellulose films is shown in Fig. 2a and b,
107 respectively (Supplementary Table 2). SEM images in Fig. 2c show the appearance of the films
108 after being in contact with nPp dispersion. The polymeric regenerated cellulose (RC) and
109 hydrophobic polystyrene (PS) films were used as reference materials (Supplementary Fig. 5). These
110 results deliver two main messages: (i) highly hygroscopic and anionic TEMPO-CNF film performs
111 the best (Fig. 2a, b) in all cases. Surprisingly, the anionic nPp are most efficiently removed by the
112 TEMPO-CNF film. (ii) Attractive electrostatic interactions seem to have a more pronounced effect
113 when dealing with μ Pp as anionic cellulose films capture cationic μ Pp in larger quantities compared
114 to anionic μ Pp (Fig. 2b).

115 As expected, due to the larger attractive energy between oppositely charged surfaces, the positively
116 charged particles are immediately attached to the anionic TEMPO CNF surface hindering the
117 particle diffusions inside the network, although not fully preventing it. In the anionic system, the
118 attractive energy between negatively charged surfaces is half of that of the oppositely charged
119 surfaces²⁸, and therefore, anionic nPp can enter inside the nanocellulose network more efficiently.
120 Indeed, TEMPO-CNF films capture approximately a third more of anionic nPp than cationic nPp.
121 The fact that TEMPO-CNF is able to efficiently capture nPp despite the particle charge is a
122 consequence of its nanoscaled porosity coupled with high hygroscopicity enabling peculiar water
123 transport properties. Once the film is in contact with aqueous solutions it swells drastically.

124 TEMPO-CNF network swelling induces capillary flow which is strong enough to transport nPp into
125 the film network. The large and active surface area of native CNF is partly lost during drying since
126 this CNF grade has a significantly lower surface charge when compared to the TEMPO-CNF. Due
127 to the lack of repulsion between the individual fibrils, upon drying, fibrils aggregate, and severe
128 hornification takes place. Hornification causes irreversible changes in fibril morphology and
129 specific surface area reducing the swelling of the fibril network and thereby lowering the water
130 uptake ability of the system.²⁷ Thus, hornification explains the lower performance of native CNF
131 films compared to TEMPO-CNF films since never-dried CNF hydrogels are able to recover
132 microplastics from water flux as discussed above (see Fig. 1). A significantly smaller area of the
133 TEMPO-CNF film (30 cm²) is needed to remove all anionic nPp from the solution when compared
134 to the native CNF film (140 cm²) (Supplementary Table 3).

135 Our results show that all films recover more of the cationic μ Pp than the anionic ones (Fig. 2b,
136 Supplementary Table 2) indicating a more pronounced role of attractive electrostatic interaction in
137 the capture process compared to the nPp system. Nanocellulose-based systems, however,
138 outperform the polymeric systems based on regenerated cellulose and polystyrene (RC and PS), due
139 to large surface area, high hygroscopicity, and possible entrapment of particles in the porous
140 network. Lignocellulose-based systems indeed can efficiently trap and transport microplastics from
141 seawater (~1500 plastic pieces/kg of seagrass) as demonstrated in the seagrass ecosystem²⁹. At best,
142 our system - also lignocellulose-derived - can collect roughly 20B nPp/mg TEMPO-CNF, which is
143 a remarkable finding. The ability of regenerated cellulose film to sieve particles cannot be fully
144 explained either by attractive electrostatic interactions, large surface area, nor water interactions
145 and, therefore, we assess the role of direct surface interactions in the capturing process.

146 **The role of interfacial interactions - Quantitative method to calculate the adsorption**
147 **parameters**

148 To further elaborate the role of surface interactions between nanoplastics and the binding substrates,
149 the adsorption of anionic nPp particles was followed using Quartz crystal microbalance with
150 dissipation monitoring (QCM-D). With this approach, we aim to exclude the influence of network
151 porosity that generates water transport functions and amplify the role of direct surface interactions.
152 We focus our interfacial investigations on colloidal-sized nPp particles since the behaviour of
153 nanoscaled particles is mostly taking place at interfaces. In nature, nanoplastics tend to accumulate
154 e.g. toxins and therefore from the environmental point of view, pure particles do not exist.⁹
155 Therefore, we used either stabilised or purified PS particles, all carrying a net negative surface
156 charge (Supplementary Table 1).

157 Our results show that anionic nPp particles - both stabilised and purified - adsorb on native CNF,
158 regenerated cellulose (RC), and on polystyrene (PS) ($\Delta f_{RC} \gg \Delta f_{CNF} > \Delta f_{PS}$) (Fig. 3a and
159 Supplementary Fig. 6 a,c) whereas no adsorption was detected on TEMPO-CNF. This result
160 indicates that the electrostatic repulsion between anionic domains prevents the direct binding of nPp
161 on the highly anionic TEMPO-CNF.

162 Finally, we introduce a systematic approach for explicit nanoplastic particle detection to bridge the
163 well-known methodological gap of detection and quantification of nPp from the environment¹⁵. We
164 qualified the substrate performance to bind colloidal plastics via surface interactions by comparing
165 the experimental surface coverage to the theoretical maximum coverage. This was carried out by
166 linking the adsorption data to comprehensive image analysis and by applying a random sequential
167 adsorption (RSA) model. In the RSA model, the jamming limit at which the density of adsorbed
168 particles (particles treated as geometrically restricted and fixed circular objects without
169 conformational and orientational changes) saturates on a 2D film is defined as a theoretical
170 maximum coverage ($\theta_{\infty} = 0.547$). Therefore, the saturation limit in RSA is significantly lower than
171 the optimum filling of the surface.^{30,31} By fitting the QCM-D data (Fig. 3a) with the RSA model
172 (Fig. 3b), and by applying the image analysis (Fig. 3c, Supplementary Fig. 7-9) we gain access to

173 the adsorption rate and the number of particles per unit area after the adsorption (dN/dt)
174 (Supplementary Table 4, Equation 2), which can be translated to surface mass density (Γ) and
175 adsorption rate ($d\Gamma/dt$) (Equation 6) since the nanoplastic adsorption process meets well the RSA
176 requirements (See Methods). QCM-D detects the adsorbed hydrated total mass by acoustic principle
177 showing simultaneously high changes in energy dissipation (Supplementary Fig. 6 b,d and 10).
178 Therefore, the simple Sauerbrey equation (Equation 1) cannot be directly used to calculate the mass
179 of the adsorbed particles. To quantify the amount of water in the adsorption process, the areal mass
180 generated from QCM-D data were rescaled utilizing the surface mass density Γ determined from the
181 SEM images by image analysis to quantify the dry mass of adsorbed nPp. Fig. 3c illustrates the
182 appearance of different substrates after the nPp adsorption process and displays the recognition of
183 particles in order to analyse the experimental coverage (θ_{max}) and maximum surface mass density
184 (Γ_{max}) via image analysis. Table 1 collects the relevant experimental data on particle adsorption, a
185 factor describing water coupled to the adsorbed layer, and surface coverage (θ_{max}) at the solid-gas
186 interface at the end of the irreversible adsorption process ($t = \sim 1h$). Table 1 also tabulates the
187 system-specific parameters from RSA fittings *i.e.* surface coverage (θ_{max}) at the solid-liquid
188 interface, the adsorption rate coefficient (k_a), and the occupied area (a) of single nPp including the
189 water, which is strongly interacting with the nanoplastic particle. It should be noted that RSA-
190 derived θ_{max} takes into account the particle diameter with coupled water resulting in higher surface
191 coverage values when compared to “dry systems”. Our results show that the strongly bound water
192 layer does not prevent the particle packing and therefore the estimation of the true surface coverage
193 ($\theta_{max}/\theta_{\infty}$) using dry system data is warranted. The full treatise of the adsorption data with the RSA
194 model is described in the Methods and Supplementary Fig. 11.

195 We extracted the key findings, and the discussion is supported by the schematic presentation shown
196 in Fig 3e. (i) Nanoplastics have the highest affinity and the highest probability (high k_a) to attach on
197 regenerated cellulose suggesting favorable surface interactions positively contributing to adsorption.

198 Particles on regenerated cellulose seem to occupy a smaller area (a) allowing a closer packing
199 density indicating that only the synergetic effect of the hydration shell and the electrical double
200 layer of the particles limit the particle packing. Approximately 50% of the theoretical surface
201 coverage maximum can be achieved within the time scale of one hour (Fig. 3d). (ii) Low anionic
202 charge of native CNF substrate promotes nPp adsorption and direct binding of particles.
203 Approximately 15% of the theoretical surface coverage maximum can be achieved with CNF, and
204 the nature of the particle - whether purified or stabilised - has only a minor influence on capturing
205 behaviour. (iii) The chemical compatibility and the hydrophobic nature of polystyrene seem not to
206 increase the probability of nanoplastics to adsorb on polystyrene. Nanoplastics have the lowest
207 adsorption probability (low k_a) on polystyrene although the probability significantly increases in the
208 purified nPp system. A circumspect explanation for the high area (a) occupied per particle at the
209 solid-liquid interface is originating from the higher amount of coupled water per adsorbed particle
210 indicated by the factor of water being 4 for polystyrene systems (Table 1). The amount of coupled
211 water (the water factor of 3) corresponds to approximately 2/3 of the experimentally sensed total
212 mass for CNF and RC surfaces and 3/4 (the water factor of 4) for the PS surface. This is in
213 accordance with other methods^{32,33}. Simultaneously, the changes in dissipation for PS systems reach
214 relatively low values suggesting the dominating role of the bulk water over the coupled water in the
215 system.

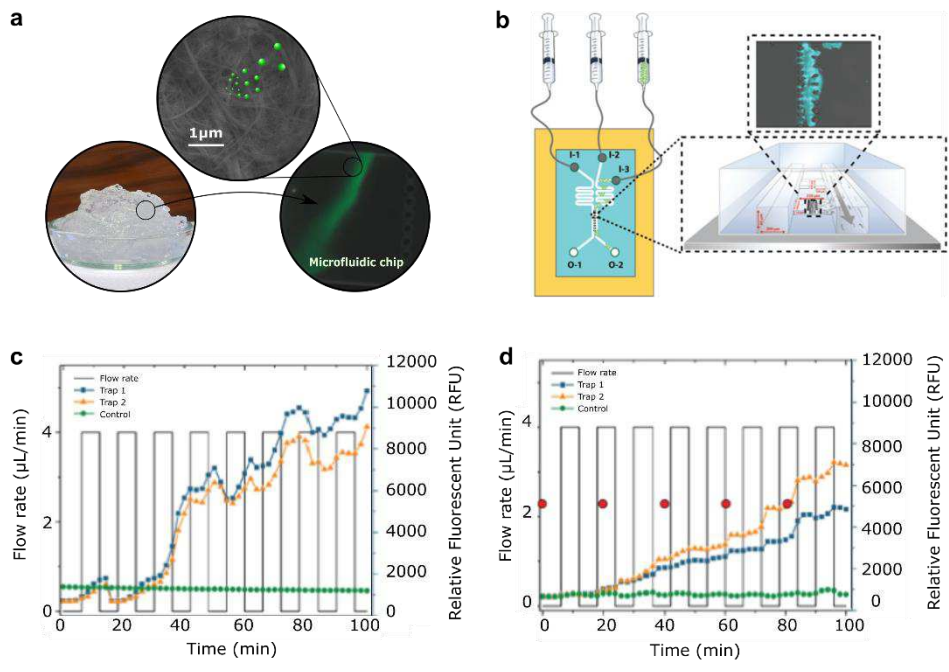
216 The adsorption behavior of nPp seems to be linked to the amphiphilic nature of cellulose³⁴,
217 especially when the electrostatic repulsion of the system is relatively weak (native CNF and
218 regenerated cellulose). Cellulosic materials have been shown to display different surface properties
219 due to the structural anisotropy³⁵. Receding and advancing contact angle values are ranging between
220 11° and 37° suggesting that that cellulose has both hydrophobic and hydrophilic domains³⁶.
221 Different wetting behavior of the cellulose surfaces has been shown to correlate with the orientation
222 of the crystal planes. The mechanism defining the nPp binding is based on the attractive surface

223 interactions only when the strong repulsive forces are not dominating and the capillary forces are
224 not assisting the capturing process.

225 **Summary**

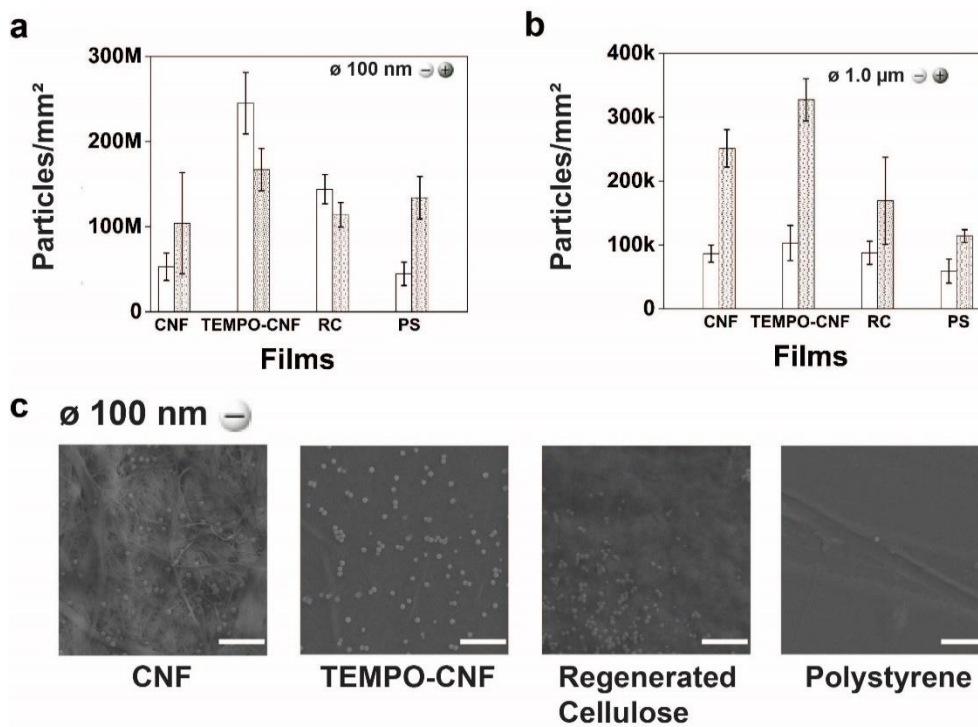
226 We introduce a universal and versatile nanocellulose-based solution, which efficiency to collect and
227 bind micro- and nanoplastic particles is not dependent on any specific physical or chemical
228 interaction. Instead, the entrapment of particles from aqueous dispersion is a result of a dual
229 synergistic feature provided by the nanocellulose network: high hygroscopicity coupled with a high
230 active surface area. These attributes enable the operational assets where colloidal plastic particles -
231 regardless of the size or surface chemistry - can be conveyed and captured inside the cellulosic
232 network by exploiting its peculiar water transport properties involving capillary forces and
233 diffusion. Once inside the network, the large surface area and favourable surface interactions
234 enhance cohesion between the particles and the surface of the material leading to efficient
235 capturing. We show that by combining surface-sensitive methods with nanomicroscopy, image
236 analysis, and modeling, we are able to quantitatively assess the nPp behavior at interfaces. This type
237 of nPp adsorption data has not been previously collected, and it is essential when designing
238 materials for quantitative analysis purposes, and for collection and recovery from different
239 environments ranging from wastewaters to the sites where the nano- and microplastics are
240 produced. Nanocellulose originates from the natural sources, it is renewable and non-toxic, which
241 are key aspects when designing next-generation functional materials diminishing the dependency on
242 the synthetic counterparts. Today, nanocellulose can be produced and modified in various ways to
243 yield hydrogels, self-standing films, and porous aerogels and cryogels, which make it an ideal
244 material for many future solutions where the high hygroscopicity is an asset^{21,37}.

245



246

247 **Figure 1. Capture of microplastic particles by native CNF hydrogel network.** **a**, Schematic illustration of a proof of
 248 concept where the capture of fluorescently labelled microplastic particles by CNF hydrogel network is verified using a
 249 microfluidic set-up and fluorescent imaging (Extended Data Video 1). **b**, Schematic illustrations of the microfluidic
 250 setup for CNF containing trap showing the injection of fluorescent nPp and μ Pp (I-3) and water (I-2/I-1). I-1 channel is
 251 used to pack the CNF hydrogel into the connected traps and I-2 is used for washing. Fluorescent accumulation of nPp
 252 (c) and μ Pp (d) over time by CNF hydrogel network. Green curves show control trap without CNF hydrogel. The
 253 orange and blue curves show parallel experiments with CNF in the traps. In **d**, the red dots indicate the time points
 254 where microscopy images were taken (Supplementary Fig. 1).



255

256

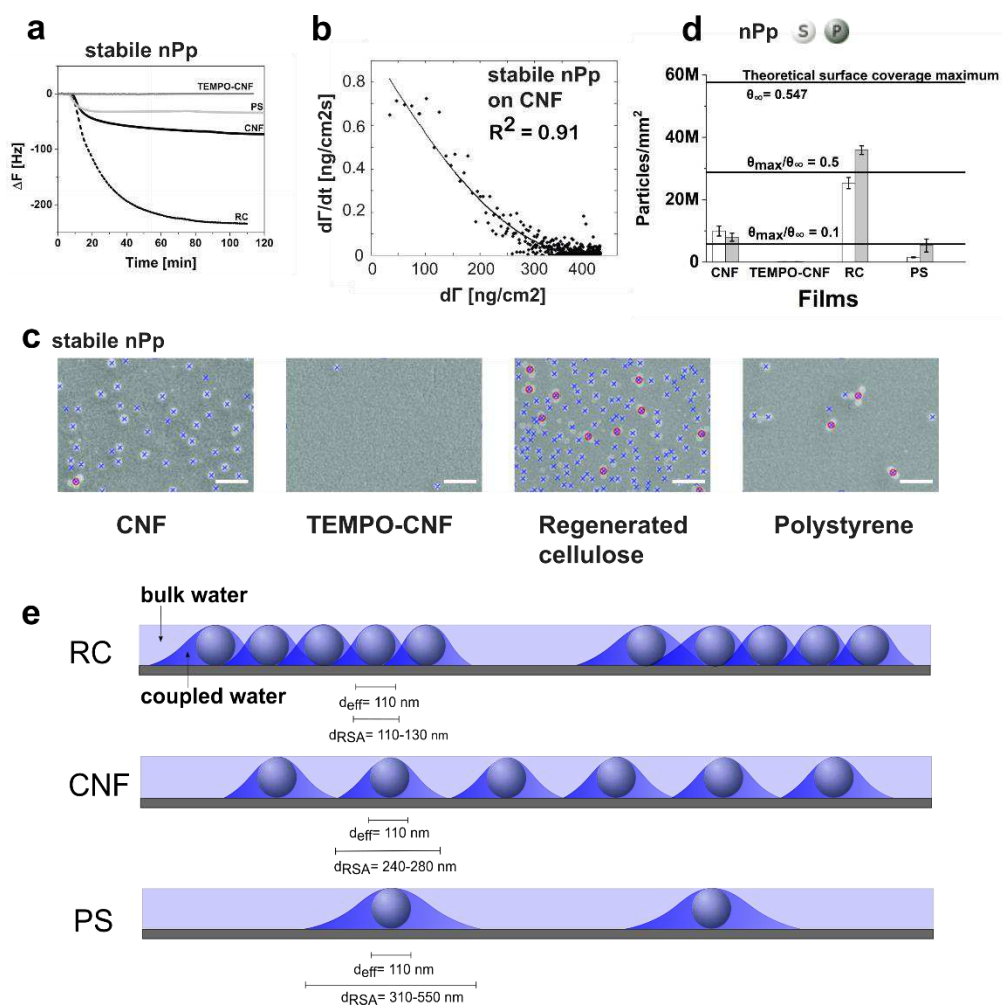
257

258

259

260

Figure 2. Quantitative assessment of entrapped fluorescent microplastic particles of different size and charge by self-standing films. a, Number of captured nPp and **b,** μ Pp calculated based on the fluorescence detection. White bars represent negatively charged plastic particles, and grey bars positively charged plastic particles. The full data for all captured particles is presented in Supplementary Table 2. **c,** SEM images of the films after being contacted with the aqueous nPp dispersion for 10 min. Scale bar in SEM images is 1 μ m.



261

262 **Figure 3. Quantitative assessment of surface binding of nPp using surface sensitive approach coupled with image**

263 **analysis and fittings with random sequential adsorption (RSA) model. a,** QCM-D frequency change responses

264 showing the adsorption of stable nPp on TEMPO-CNF (dark gray line), PS (grey line), native CNF (solid black line),

265 and RC (dashed black line). **b,** Fitting of the QCM-D adsorption data of stable nPp on CNF using the RSA model.

266 Black dots are measured data, and black line is the RSA fit. The adjusted R^2 for the fit is 0.91. **c,** Stable nPp

267 recognition from scanning electron microscopy (SEM) images using image analysis (Supplementary Fig 9). The SEM

268 image scale bar is 0.5 μm . **d,** Amount of nPp detected after the adsorption experiments (white bars stable, grey bars

269 purified) via image analysis of SEM micrographs contrasted to a theoretical surface coverage maximum ($\theta_\infty = 0.547$

270 which equals to $\sim 5.8 \times 10^{-7}$ circles mm^2), which is based on the RSA model. **e,** Schematic presentations display the

271 appearance of substrates at the end of the nPp adsorption process showing the existence of bulk water and water which

272 is strongly interacting with nPp. d_{eff} describes the effective particle diameter, and d_{RSA} is the diameter of the occupied

273 area (a) of a single nPp including the particle and the coupled water.

274

275

276

277 **Table 1** Experimental data, adsorption parameters and surface coverage estimations for different nPp systems.

	Experimental data					RSA fitting parameters				
	QCM Δf_5 (Hz) ^a	QCM ΔD_5 ($\times 10^{-6}$) ^a	Coupled water ^b $\frac{\Delta f_5(QCM)}{\Delta f_5(IA)}$	Γ_{max} (ng cm^{-2}) ^c	θ_{max} (solid/air) ^d	θ_{max} (solid/liquid) ^e	$a \times 10^4$ (nm^2) ^f	d_{RSA} (nm) ^g	$k_a \times 10^{-5}$ (cm s^{-1}) ^h	$\frac{\theta_{max}}{\theta_{\infty}}$ ⁱ
CNF + 	-75	21	3.2	419	0.076	0.48	6.0	280	1.0	0.14
CNF + 	-92	24	3.1	524	0.095	0.45	4.5	240	1.2	0.17
RC + 	-230	38	3.1	1330	0.24	0.35	1.4	130	1.6	0.44
RC + 	-340	47	3.2	1890	0.34	0.34	1.0	110	1.9	0.62
PS + 	-19	5.4	4.2	80.7	0.015	0.36	24	550	0.2	0.027
PS + 	-67	14	4.2	281	0.051	0.36	7.6	310	1.2	0.093

278 ^a Changes in frequency and dissipation at the end of the QCM-D measurement after the rinsing step.279 ^b Estimation of the amount of water detected at the end of nPp adsorption (see Methods).280 ^c Maximum surface mass density gained from SEM images and image analysis.281 ^d Maximum experimental surface coverage at the end of the adsorption experiment at solid/gas interface determined by
282 image analysis. Particle amount on the surface compared to the theoretical maximum amount calculated based on the
283 RSA model assuming that $\theta_{\infty} = 0.547$.284 ^e Maximum experimental surface coverage at the end of adsorption at solid/liquid interface calculated using Equation 4,
285 where area a is obtained from RSA fitting.286 ^f Occupied area of a single nanoplastic particle including particle and the coupled water i.e. water strongly interacting
287 with the particle288 ^g Diameter of the area (a) taken by the particle and coupled water289 ^h Adsorption coefficient describing the affinity of nPp towards the surface obtained from RSA fitting.290 ⁱ Fractional surface coverage, where $\theta_{\infty} = 0.547$ is the theoretical maximum surface coverage based on the RSA model.
291 When analyzing the adsorption of purified nPp on RC substrate, Equation 3 is valid when $\theta_{max} < 0.3$. Since θ_{max} for RC
292 is > 0.3 , the Equation 5 was applied. If applying the Equation 6, d_{RSA} would be 96 nm, which is an underestimate since
293 $d_{eff} = 110$ nm.

294

295

296

297

298

299 **METHODS**

300 **Polystyrene particles**

301 Fluorescently labeled polystyrene (PS) particles (L9902, L9904, L4655, and L9654 from Sigma
302 Aldrich) of different size and surface charge (cationic and anionic) were used to analyze
303 microplastic capturing ability, and to reveal the capturing mechanisms of CNF hydrogel and self-
304 standing films. Particles with diameters of 100 nm and 1.0 μm (i.e. nanoplastic particles **nPp** and
305 microplastic particles **μPp** , respectively) were used. Later referred to as fluorescently labeled nPp or
306 μPp or fluorescently labeled particles if both sizes are discussed.

307 Colloidal sized PS particles (LB1 from Sigma Aldrich) were utilized for QCM-D experiments ($\phi =$
308 100 nm, i.e. nPp). These particles were utilized in a **stable** form (i.e. utilized as provided by the
309 supplier) or **purified** with the supplier's protocol to remove most of the stabilising agent. Stable
310 particles represent the native state of nanoplastics. Surface charges for the stable and purified
311 particles were determined by zeta potential measurements (Supplementary Table 1).

312 **Nanocellulose materials**

313 Two different grades of cellulose nanofibrils were utilized: mechanically disintegrated cellulose
314 nanofibrils (native CNF)²⁴ and TEMPO-oxidized (TEMPO = 2,2,6,6-tetramethyl-1-piperidinyloxy
315 radical) cellulose nanofibrils (TEMPO-CNF).²⁶ These two nanocellulose materials vary in fibril
316 diameter, surface roughness, and water contact angle (Supplementary Fig. 5). Mechanically
317 disintegrated CNFs were prepared from never dried bleached birch kraft pulp obtained from the
318 Finnish pulp mill. The pulp was first soaked at 1.7 wt% consistency and dispersed using a high
319 shear Diaf dissolver (Minibatch Type20) for 10 min at 700 rpm. The pulp suspension was pre-
320 refined in a Masuko grinder (Supermasscolloider MKZA10-15J, Masuko Sangyo Co., Japan) at

321 1500 rpm and fluidized with six passes through a Microfluidizer (Microfluidics M-7115-30
322 Microfluidics Corp.). The mechanical disintegration resulted in a viscous gel with a final solid
323 content of ~1.6 wt% with an anionic charge of 0.04 mmol g⁻¹ analysed by conductometric titration
324 (SCAN 65:02).

325 TEMPO-oxidized cellulose nanofibrils (TEMPO-CNF) were produced from bleached softwood
326 kraft pulp obtained from the Finnish pulp mill. Prior to the fibrillation, the pulp was TEMPO-
327 oxidized according to a protocol described by Saito et al.²⁶ Shortly, the never-dried bleached
328 softwood pulp was oxidized with NaClO mediated by 2,2,6,6-tetramethylpiperidine-1-oxyl
329 (TEMPO, Sigma Aldrich). The degree of oxidation per anhydroglucose unit was 1.3 mmol g⁻¹,
330 determined by conductometric titration (SCAN 65:02). The washed TEMPO-oxidized pulp was
331 subsequently fibrillated with a high-pressure fluidizer (Microfluidics M110P, Microfluidics Int.
332 Co., Newton, MA) with two passes. The final solid content was 1 wt%.

333 **Microfluidistic set-up and fluorescence microscopy**

334 The capacity of native CNF hydrogel to capture microplastic particles (fluorescently labeled) was
335 followed using a microfluidic setup and fluorescence microscopy. Microfluidic chips were designed
336 and prepared by standard soft lithography and replica molding approach as previously described³⁸.
337 Initially, a master mold including photoresist SU-8 (MicroResist GmbH) on a silicon wafer was
338 created by spin coating two distinct layers, SU-8-5 for the 1.6 μm layer and SU-8-50 for the 20 μm
339 layer. Each layer was exposed to a mercury lamp i-line (3 & 8.5 seconds, respectively). After
340 development of the topographies, the surface was coated with a ~20 nm fluorocarbon polymer film
341 to facilitate the removal of the PDMS replica after molding³⁹. PDMS was prepared by mixing the
342 monomer and crosslinking agent in 10:1 ratio (Sylgard 184 kit, Dow Corning), degassing it, casting
343 it on the microfluidic mold, followed by an overnight curing step at 70°C. Chips were bonded to
344 glass coverslips by oxygen plasma treatment.

345 CNF dispersion of 0.5 wt% was prepared for the microfluidic experiments. Before loading the
346 microfluidic channels, the 0.5 wt% CNF solution was centrifuged for 5 min to spin down large
347 fibrils. The supernatant was loaded into the microfluidic chips with a 500 μ l syringe through a
348 single channel, with a flow rate of 300 μ m s⁻¹. After the CNF fibrils entangled behind the pillars to
349 form a solid transparent membrane, the CNF solution was switched to H₂O. Phase-contrast and
350 fluorescent images were acquired using an Axio Observer Z1 microscope (Carl Zeiss, Jena,
351 Germany)⁴⁰. Images were acquired every two minutes at 20x magnification during the experiment.
352 The fluorescent signal was obtained from the fluorescent 100 nm and 1.0 μ m particles using
353 excitation light at 480 nm, while collecting the emitted light from 515-535 nm. The flow was
354 continually switching between the wash solution (Channel B) and the microplastic particle solution
355 (Channel C) every six minutes.

356 A cross-section profile fluorescence intensity analysis of the CNF hydrogel network was performed
357 on 4 individual traps for each condition in order to gain understanding of the penetration of nPp and
358 μ Pp into the CNF hydrogel network. Cross-sections were acquired in the middle of the washing
359 cycle at 86 min, to ensure only entrapped and bound particles were considered in the analysis.
360 Fluorescence reads were scaled against its peak fluorescence, after which the area under the curve
361 was calculated (Δx 400 nm) and plotted against the distance of the trapped nPp and μ Pp.

362 **Preparation of self-standing films**

363 Native CNF films were prepared from 0.8 wt% gel, which was cast on polystyrene Petri dishes (\varnothing 9
364 cm) and dried under ambient conditions for 24 hours. The formed CNF films were separated from
365 the plastic supports for further experiments.

366 TEMPO-CNF films were prepared from 0.2 wt% gel, which were cross-linked with polyvinyl
367 alcohol (PVA, Mowiol 56-98, M_w 195 000g/mol) according to previously described procedure⁴¹ to
368 enhance the films' wet strength. TEMPO-CNF gel was cast on polystyrene Petri dishes (\varnothing 9 cm)

369 and dried under ambient conditions for 24 hours. The formed TEMPO-CNF films were separated
370 from the plastic supports for further experiments. The weight of 1.5 cm x 1.5 cm film was on
371 average 0.0047 g.

372 RC film was prepared by dissolving microcrystalline cellulose powder from spruce (Fluka) in ionic
373 liquid (EMIM[OAc], IoLiTec GmbH) to a 10 wt% solution under heat and mixing. Subsequently, a
374 film was cast on a glass surface using a 510 Coatmaster film applicator (ERICHSEN GmbH & Co.
375 KG, Hemer, Germany) with a gap of 400 μm and speed of 40 mm s^{-1} . The regeneration was carried
376 out by immersing the cellulose in water for 1.5 hours. Finally, the regenerated cellulose film was
377 placed between absorbent papers and air-dried at ambient conditions for 3 days.

378 PS film was prepared by dissolving PS pellets (Mw 192,000 g/mol, Sigma Aldrich) in toluene to a
379 10 wt% solution at ambient conditions overnight. The PS solution was cast on a glass Petri dish and
380 air-dried at ambient conditions for 12 hours. The formed PS film was separated from the glass
381 support for further experiments.

382 **Fluorescence spectroscopy**

383 Quantification of fluorescently labeled anionic and cationic particles captured by self-standing films
384 was conducted using a Cary Eclipse fluorescence spectrophotometer (Varian Scientific Instruments,
385 CA, USA). Fluorescently labeled particles were dispersed to a final concentration of 0.1 g L^{-1} in
386 phosphate buffer (10 mM, pH 6.8). The calibration curves were recorded from five concentrations
387 (0, 0.025, 0.05, 0.075, and 0.1 g L^{-1}) for each fluorescent particle at their specific emission maxima
388 (Supplementary Fig. 12). Fluorescence studies were carried out by immersing the films in the
389 aqueous dispersion containing 0.1 g L^{-1} particles for 10 min without mixing (Supplementary Fig. 4).
390 The fluorescence of the solutions was recorded before and after the immersion. The amount of
391 recovered particles was calculated by subtracting the fluorescence value after immersion from the

392 fluorescence before the film immersion. All measurements were performed in triplicate with three
393 readings each.

394 The number of particles captured by the films equals to the total mass recovered (m_{Tot}) divided by the
395 single-particle mass ($m_{particle}$). Above $m_{Tot} = cV$, where c is the measured concentration, and V is the
396 known volume. The mass of a single PS particle ($m_{particle} = 5.49 \times 10^{-7}$ ng) was calculated, assuming
397 it to be a sphere with a density of $\rho = 1.05$ g cm⁻³ (ρ of PS particles is provided by the supplier).

398 **Preparation of ultrathin films for adsorption investigations**

399 Native CNF, TEMPO-CNF, RC, and PS ultrathin films were prepared by spin coating (Model WS-
400 400BZ-6NPP/LITE, Laurell Technologies, North Wales, PA, USA) the materials on QCM-D sensor
401 crystals (AT-cut quartz crystals with Au or SiO₂ surfaces supplied by Q-Sense, Gothenburg,
402 Sweden). The crystals were rinsed with Milli-Q water, dried with nitrogen gas and placed in a UV-
403 ozonizer (Bioforce Nanosciences, CA) for 10 min to clean the surfaces. Prior to CNF or TEMPO-
404 CNF deposition, a layer of anchoring polymer (polyethylene imine (PEI), 30 wt%, Mw 50,000-
405 100,000 g/mol, Polysciences Inc.) was adsorbed onto the crystal surface by immersing the crystal in
406 1 g L⁻¹ PEI solution for 30 min. The excess of PEI was rinsed away with large amounts of Milli-Q
407 water, followed by nitrogen gas drying.

408 Transparent dispersion of CNF for spin coating was prepared as described by Ahola et al.⁴² Briefly,
409 CNF gel was ultrasonicated (400 W tip sonicator, Branson 450 Digital Sonifier, Branson
410 Ultrasonics, Danbury, USA) for 10 min with 25 % amplitude. Subsequently, larger fibril bundles
411 were removed by centrifugation (10400 rpm, 45 min). The supernatant with the individual fibrils
412 was collected by pipetting. The Au-coated sensor surface with PEI was first wetted by spin coating
413 100 μ l of Milli-Q water on the sensor at 3000 rpm for 10 s. Subsequently, the individualized
414 nanofibrils were spin coated (3000 rpm, 90 s) on the QCM-D sensor surfaces. After spin coating,

415 the surfaces were rinsed with water, dried gently with nitrogen gas and placed in an oven for heat-
416 treatment (80 °C, 10 min).

417 Ultrathin films of TEMPO-CNF were prepared with a protocol described by Hakalahti et al.²³.
418 TEMPO-CNF surfaces were prepared from 0.15 wt% TEMPO-oxidized CNF solution, which was
419 ultrasonicated for 2 min with 25 % amplitude to break down aggregates. Before spin coating of
420 TEMPO-CNF the Au-coated sensor surface with a thin PEI layer was wetted by spin coating 100 µl
421 of Milli-Q water on the sensor at 3000 rpm for 10 s. Subsequently, the nanofibrils were spin coated
422 (3000 rpm, 90 s) onto the QCM-D crystals. After spin coating, the surfaces were rinsed with water,
423 dried gently with nitrogen gas, and placed in an oven for heat-treatment (80 °C, 10 min).

424 RC surfaces were prepared from trimethylsilyl cellulose (TMSC) ultrathin films by desilylation.
425 TMSC was synthesized by silylation of cellulose powder with hexamethyl disilazane (HDMS), as
426 described previously.⁴³ Dried TMSC was dissolved into toluene to form a 10 g L⁻¹ solution. Prior to
427 spin coating the TMSC, the surface of the SiO₂-coated sensor surface was wetted by applying 5
428 droplets of toluene and spun with the speed of 3000 rpm for 15 s. The TMSC solution was
429 subsequently spin coated onto SiO₂-sensor (3000 rpm, 60 s). The solvent was evaporated by placing
430 the crystals in the oven (60 °C, 10 min). The TMSC ultrathin films were regenerated back to
431 cellulose by desilylation with hydrochloric acid vapor, producing ultrathin RC films.

432 PS ultrathin films were prepared from a polystyrene solution (0.1 wt% polystyrene in toluene) by
433 spin coating on a gold QCM-D crystal (4000 rpm, 30 s). The solvent was evaporated in the oven (60
434 °C, 10 min). All coated QCM-D crystals were stored in desiccators.

435 **Atomic force microscopy (AFM)**

436 Sufficient coverage of the ultrathin films on QCM-D sensors was verified by AFM using a NanoTA
437 AFM+ instrument (Anasys Instruments, Bruker, MA, USA) with Mounted Standard Silicon

438 Tapping Mode Probes with Al Reflex coating (Applied Nanostructures Inc., CA, USA). Images of
439 the ultrathin film surfaces were recorded in tapping mode in the air with a scan rate of 0.5 Hz with
440 silicon cantilevers. The damping ratio was around 0.7-0.85 Hz. For each sample, three different
441 areas were analyzed, and the images were not processed by any other means except flattening. AFM
442 images of all ultrathin film surfaces and their height profiles are presented in Supplementary Fig. 4.

443 **Water Contact angles (WCA)**

444 WCAs for ultrathin films were determined to assess the films' chemical nature. We used a sessile
445 drop method with a video camera-based fully computer-controlled contact angle meter (Attension
446 Theta Optical Tensiometer, Biolin Scientific, Finland). A droplet volume of 2 μl (Milli-Q water)
447 and a recording time of 120 s were used to measure the contact angle of the ultrathin films. 2-3
448 droplets were applied on the ultrathin film surfaces, and the average contact angles were calculated
449 from these. The values used for the calculations were from time point 1.4 s. The value was taken
450 from the beginning of the measurement since the droplet is affected by evaporation due to its small
451 size. WCA values are shown in Supplementary Fig. 3 for all ultrathin films on the upper part of the
452 AFM image.

453 **Quartz Crystal Microbalance with Dissipation (QCM-D)**

454 Adsorption of PS particles (LB1, LB11) on native CNF, TEMPO-CNF, RC, and PS ultrathin films
455 was investigated using E4 QCM-D instrument (Q-Sense AB, Gothenburg, Sweden). QCM-D is
456 used for following *in situ* changes of mass at solid/gas and solid/liquid interface, since the measured
457 change in frequency (Δf) corresponds to the change in areal mass (Δm). Simultaneously the change
458 in dissipation (ΔD) is monitored yielding information on the changes in viscoelastic properties of
459 the adsorbed layer. The interpretation of QCM-D data is described elsewhere in detail.⁴⁴ If the
460 adsorbed film is evenly distributed and rigid, the change in frequency is directly proportional to the

461 change in areal mass and can be calculated according to the Sauerbrey relation presented in
462 Equation 1⁴⁵.

$$463 \quad \Delta m = -\frac{C}{n} \Delta f \quad (1),$$

464
465 where Δm is the areal mass, n is the overtone number ($n = 1, 3, 5, 7, 9, 11$), and $C = 17.7 \text{ ng (cm}^{-2}$
466 $\text{Hz}^{-1})$ for the 5 MHz AT-cut crystal. Changes in dissipation must remain low ($<10^{-5}$) for the
467 Sauerbrey equation to remain valid. Larger changes indicate a softer and thicker layer, where the
468 amount of adsorbed water is significant.

469 PS particle adsorption experiments were carried out as follows. Purified and stable 0.1 g L^{-1} PS
470 particle ($\phi = 100 \text{ nm}$, nPp) dispersions were prepared in phosphate buffer (10 mM, pH 6.8). QCM-
471 D sensor surfaces coated with ultrathin films were stabilised in the buffered conditions for at least
472 12 hours. Before introducing PS particle dispersion to the QCM-D chamber, the sensor surfaces
473 were contacted with the phosphate buffer solution for approximately 1 hour to avoid the bulk effect.
474 Then 0.1 g L^{-1} PS particle dispersion was introduced into the QCM-D chamber with the flow rate of
475 0.1 ml min^{-1} for approximately 1 hour. The particle adsorption was confirmed by rinsing the surface
476 with phosphate buffer for 1 h. Two replicates of each measurement were performed. The adsorption
477 of PS particles, as well as the possible desorption due to rinsing were monitored by following the
478 changes in frequency (Δf) and dissipation (ΔD) as a function of time.

479 **Scanning Electron Microscopy (SEM) and image analysis**

480 Self-standing and ultrathin films were imaged after fluorescence and QCM-D measurements with a
481 Merlin Field Emission (FE)-SEM (Carl Zeiss NTS GmbH, Germany) to visualize the films after
482 particle capture and adsorption. The self-standing films and QCM-D crystals were dried after the
483 measurements and attached onto SEM sample holders using carbon tape. Samples on the holders

484 were coated with gold by sputtering (2 nm thick gold surface) to improve sample conductivity.
485 Samples were imaged with the electron gun voltage of 3-5 kV and the grid current of 60 pA. The
486 number of pixels in the SEM image was 2048 (H) x 1536 (V), with 256 gray levels. At least three
487 SEM images of each sample were acquired at different positions. In addition, the number of
488 adsorbed PS particles on the ultrathin films was quantified using image analysis, which was
489 developed to recognize the PS particles in SEM images to determine the particle amount per mm².

490 In SEM imaging, as in imaging methods general, images are clipped within a rectangular boundary.
491 When a spatial pattern is observed through a rectangular clipping window, several edge defects
492 arise. One of these edge defects is size-dependent sampling bias. Miles has discussed plus-sampling
493 (any object that intersects the clipping window is accepted) and minus-sampling (only those objects
494 that lie within the clipping window are accepted).⁴⁶ In our research, no attempt was made to
495 determine the particle size distribution as the particles in the image were the same size. Therefore,
496 size-dependent sampling bias was not a problem in our analysis. The relationship between the
497 actual dimensions of the particles (μm) and the pixel size of the particles was obtained from the
498 scale bar in the SEM image. The SEM images were of good quality; the background variation was
499 small and bright objects (particles) stood out clearly from the dark background. Therefore, no image
500 preprocessing was required, and the first image processing operation was segmentation. It was
501 possible to use a global threshold value because the background variation was small. The
502 thresholding method used in this study was based on histogram shape information. The threshold
503 was chosen for the descending part of the prominent peak of the histogram (see Supplementary Fig.
504 9). The aim was to identify the individual PS particles and their centers, making it possible to
505 determine the total number of particles. In most SEM images, the particles were detached from each
506 other or formed only small clusters. However, in some cases, the particles had a strong tendency to
507 form clusters (Examples of SEM images with identified particles shown in Supplementary Fig. 8).
508 Thus, the next step of the image analysis was divided into two methods depending on which of the

509 above categories the image was classified into. When the particles were mainly detached, the
510 particles were identified from the threshold image by their area (we know the diameter of particle
511 size in each image) and shape (circular objects). The size of the clusters observed was assumed to
512 be three particles. In samples where the clusters were large, and the particles were mainly in the
513 clusters, individual particles were not reliably identified. In this case, the area of each cluster was
514 determined, and the number of particles needed to achieve the same area was calculated. Finally,
515 the identified particles were presented by drawing a marker on the original SEM image (see
516 Supplementary Fig. 8, 9).

517 **Theoretical maximum adsorption of particles - Fittings with RSA model**

518 We used random sequential adsorption (RSA) model to evaluate the maximum adsorption capacity
519 of the ultrathin films. The thickness of the ultrathin film is well below 100 nm. Thus, the PS
520 particles cannot penetrate the film. If the goal is to determine the maximum number of PS particles
521 that can fit on the surface of ultrathin films, the question can be simplified to the packing of circular
522 disks in a plane. Adsorption of particles on solid, flat surfaces is often an irreversible process, as
523 was also verified by QCM-D measurements in this study (Supplementary Fig. 6). In addition,
524 particles usually do not adsorb one on top of each other, instead they form a monolayer
525 (Supplementary Fig. 7). The basic RSA model assumes that only steric repulsion is present between
526 the circular disks. For circular disks of the same size, saturation occurs at a surface coverage θ_∞ of
527 0.547. If there are disks of different sizes (particles of varying diameter) in the system, higher
528 surface coverage θ can be reached. In this study, all particles were the same size. If the viewing area
529 is one mm^2 and the PS particles are the same size, the maximum area covered by the particles is
530 0.547 mm^2 . In this case, a 1 mm^2 area can hold 5.76×10^7 circles (PS particles) with an effective
531 diameter (diameter that perceives also the estimation of electrical double layer and hydration shell
532 of the particle) of $d_{\text{eff}} = 1.1d_{\text{abs}} = 110 \text{ nm}$.⁴⁷ The cross-sectional area of one particle was calculated
533 using $A_{\text{particle}} = \pi(d_{\text{eff}}/2)^2$. Also the RSA model assumes that particles hit the surface at the same rate

534 throughout the adsorption process⁴⁸. Therefore, the concentration c must be high enough to form a
535 monolayer in the saturation regime. If there are not enough particles, the adsorption process may
536 stop before reaching the saturation surface coverage. Table 1 shows that the maximum surface mass
537 density (Γ_{max}) was 1890 ng cm⁻² for purified nPp adsorbed on RC. With a QCM-D sensor diameter
538 of 9 mm, there was ~1200 ng of nPp on the sensor surface. This corresponds to approximately 0.2%
539 of nPp (100 000 ng cm⁻³ nPp dispersion was introduced into the QCM-D chamber with a flow rate
540 of 0.1 ml/min for approximately 1 hour). Therefore, we can assume that nPp hit the surface at the
541 same rate throughout the adsorption process, and the requirements to utilize the RSA model are
542 met. In our system, all of the main RSA principles are valid, and therefore, the adsorption
543 behaviour of nPp particles can be described using the random sequential adsorption (RSA) model.³¹

544 **Assessment of particle adsorption kinetics and the amount of coupled water**

545 In order to evaluate the kinetics of the PS particle adsorption process, we modeled the QCM-D data
546 (Fig. 3a, Supplementary Fig. 6) with the RSA model (Fig. 3b) with input value for number of
547 particles gained from the image analysis. The kinetics of adsorption of particles can be described by
548 equation 2.⁴⁸⁻⁵⁰

$$549 \quad \frac{dN(t)}{dt} = k_a c' B(\theta) - k_d \theta \quad (2)$$

550 Where $N(t)$ is the number density of adsorbed particles (in units of 1 cm⁻²), θ is the surface coverage
551 $\theta=[0,1]$, t is the adsorption time (s), k_a is the adsorption rate coefficient (cm s⁻¹), k_d is the desorption
552 coefficient (cm s⁻¹), $B(\theta)$ is the surface blocking function, and c' is the particle number concentration
553 (no. cm⁻³). The adsorption of polystyrene particles on a solid surface is often an irreversible process,
554 which can be described using the RSA model ($k_d=0$). According to Shaaf and Talbot³¹, the surface
555 blocking function $B(\theta)$ in the RSA model can be expressed as

556
$$B(\theta) = 1 - 4\theta + \frac{6\sqrt{3}}{\pi} \theta^2 + \left(\frac{40}{\pi\sqrt{3}} - \frac{176}{3\pi^2} \right) \theta^3. \quad (3)$$

557 The surface coverage θ can be represented by

562
$$\theta = \frac{\Gamma a}{m}, \quad (4)$$

558 where a is the occupied area of a single particle (cm^2), m is the mass of a single particle [ng], and Γ
 559 is the adsorbed mass per unit area (ng cm^{-2}). Equation 3 is valid for $\theta < 0.3$.^{31,49} At higher surface
 560 coverage, the kinetics can be approximated with equation 5.⁴⁹ Near the jamming limit ($\theta_\infty = 0.547$)
 561 K_0 is about 8.98.

563
$$B(\theta) = K_0(\theta_\infty - \theta)^3 \quad (5)$$

564 Noting that $\Gamma(t) = N(t)m$, $c = c'm$ (c in units of ng cm^{-3}), and combining equations 2, 3, and 4 we get,

565
$$\frac{d\Gamma(t)}{dt} = k_a c \left(1 - 4\Gamma \frac{a}{m} + \frac{6\sqrt{3}}{\pi} \left(\Gamma \frac{a}{m} \right)^2 + \left(\frac{40}{\pi\sqrt{3}} - \frac{176}{3\pi^2} \right) \left(\Gamma \frac{a}{m} \right)^3 \right). \quad (6)$$

566 The goal was to determine the adsorption coefficient k_a (cm s^{-1}) and the occupied area per nPp a
 567 (cm^2). Supplementary Fig. 5a shows the frequency change determined by QCM-D for the
 568 adsorption of stabile nPp from a solution with a concentration (c) of 0.1 g L^{-1} ($100\,000 \text{ ng cm}^{-3}$)
 569 onto different surfaces. Adsorbed mass was calculated using Equation 1. All analysis was based on
 570 the 5th overtone (25 MHz , $f_0 = 5 \text{ MHz}$, $n = 5$). The RSA fittings were performed using Matlab's
 571 Curve Fitting Toolbox. Equation 6 was the custom equation. Trust-Region algorithm was used with
 572 the following coefficient starting points $k_a c = (a/m) = 0.1$. Lower and upper bounds for both
 573 coefficients were 0 and 10. Because QCM-D measurement detects both water and nanoplastic
 574 particles adsorbed on the sensor surface, QCM-D was combined with a direct observation method
 575 (SEM imaging coupled with image analysis) to obtain the adsorbed dry mass. The amount of
 576 adsorbed nPp was calculated from SEM images of dry ultrathin films after the adsorption

577 measurements. SEM images were then analyzed as described above, and the number of particles
 578 was determined. Since the mass of a single nanoplastic particle was known (5.26×10^{-7} ng) the total
 579 dry mass can be calculated (Δm_{IA}) which equals to the surface mass density Γ (ng cm⁻²). To
 580 eliminate the influence of water on QCM-D measurement, the QCMD-D data $m(t)$ were rescaled
 581 utilizing the surface mass density (Γ) determined from the SEM images ($\Gamma(t) = m(t) * (\Gamma_{max}/m_{max})$)
 582 where max refers to the maximum value determined by each measurement method.

583

584 To estimate the amount of coupled water (water strongly interacting with the nPp particles) the total
 585 dry mass of particles at the end of the adsorption process (analysed via image analysis) was first
 586 translated into theoretical frequency change ($\Delta f(IA)$) by applying the Equation 1. Secondly, the
 587 true frequency changes ($\Delta f(QCM)$) obtained from the QCM-D measurements were compared with
 588 the theoretical frequency changes to reveal the amount of adsorbed water as exemplified in the
 589 following calculation:

590

591 Example calculation for determining the theoretical frequency response for CNF surface with
 592 adsorbed purified 100 nm particles for the 5th overtone and comparing it to the non-normalized
 593 frequency response from the QCM-D measurement.

$$594 \quad \Delta f_5(IA) = -\frac{\Delta m_{IA} * n}{C} = \frac{419 \frac{ng}{cm^2} * 5}{17.7 \frac{ng}{cm^2} * Hz} = -118.5 Hz$$

$$595 \quad \frac{\Delta f_5(QCM)}{\Delta f_5(IA)} = \frac{-373.5 Hz}{-118.5 Hz} = 3.15 \dots \approx 3.2$$

596

597 For CNF and RC surfaces and both particle types (purified and stable) the frequency response was
 598 a factor of 3 larger for the experimental frequency compared to the calculated frequency from
 599 image analysis. This result indicates that 2/3 of the sensed mass by the QCM-D 5th overtone
 600 frequency corresponds to the coupled water. For PS ultrathin film, the result was that 3/4 of the

601 sensed mass by QCM-D was coupled water. According to previous studies, the difference between
602 the hydrated and dry mass is typically a factor of 1.5-40³². The factor in the case of adsorbing nPp is
603 in the lower range since QCM-D is typically used to study protein adsorption, where the proteins
604 can be thought as soft spheres, including water in their structure. In contrast, in the case of nPp they
605 are hard spheres with water only on the surface. Thus, the amount of water that adsorbs along the
606 particles is smaller than for proteins.

607

608 Acknowledgements

609 This work has been done as a part of the Academy of Finland's Flagship Programme under Projects
610 No. 318890 and 318891 (Competence Centre for Materials Bioeconomy, FinnCERES). SA has
611 been funded by the Academy of Finland's postdoctoral project No. 311608/326262 (BoNC-Fi). We
612 thank Katja Pettersson for technical assistance with AFM imaging.

613 Author contributions

614 IL performed the QCM-D experiments and SEM imaging for image analysis. IL performed the
615 sample preparation and necessary characterizations for all measurements. IL contributed to the
616 interpretation of all data and wrote the first version of the manuscript with the co-authors and
617 participated in finalizing it. TL (VTT) conducted the image analysis and RSA fittings, interpreted
618 RSA data and wrote the respective parts. TL (Aalto/VTT) executed the fluorescent experiments
619 with self-standing films. CJ executed the fluorescent microscopy experiments with hydrogels. SA
620 planned and supervised experimental work of IL, TL, and CJ. SA interpreted and handled
621 fluorescent and QCM-D data. SA wrote the first version of the manuscript with the co-authors and
622 prepared the figures. TT initiated the research concept, contributed to the experimental planning,
623 supervised the interpretation of all data and finalized the manuscript. All authors approved the
624 manuscript.

625 Competing interests

626 The authors declare no competing interests.

627 References

- 628 1. Galloway, T. S. & Lewis, C. N. Marine microplastics spell big problems for future
629 generations. *Proc. Natl. Acad. Sci.* **113** (9), 2331–2333 (2016).
- 630 2. Wright, S. L. & Kelly, F. J. Plastic and Human Health: A Micro Issue? *Environ. Sci.*
631 *Technol.* **51**, 6634–6647 (2017).
- 632 3. Ivleva, N. P., Wiesheu, A. C. & Niessner, R. Microplastic in Aquatic Ecosystems. *Angew.*
633 *Chemie - Int. Ed.* **56**, 1720–1739 (2017).
- 634 4. Jambeck, J. R. *et al.* Plastic waste inputs from land into the ocean. *Science* **347**, 768–71
635 (2015).
- 636 5. Gigault, J. *et al.* Current opinion: What is a nanoplastic? *Environ. Pollut.* **235**, 1030–1034
637 (2018).
- 638 6. da Costa, J. P., Santos, P. S. M., Duarte, A. C. & Rocha-Santos, T. (Nano)plastics in the
639 environment - Sources, fates and effects. *Sci. Total Environ.* **566–567**, 15–26 (2016).
- 640 7. Chae, Y. & An, Y. J. Effects of micro- and nanoplastics on aquatic ecosystems: Current
641 research trends and perspectives. *Mar. Pollut. Bull.* **124** (2), 624–632 (2017).
- 642 8. Ragusa, A. *et al.* Plasticenta: First evidence of microplastics in human placenta. *Environ. Int.*
643 **146**, (2021).
- 644 9. Zhang, C., Chen, X., Wang, J. & Tan, L. Toxic effects of microplastic on marine microalgae
645 *Skeletonema costatum*: Interactions between microplastic and algae. *Environ. Pollut.* **220**,
646 1282–1288 (2017).

- 647 10. Al-Sid-Cheikh, M. *et al.* Uptake, whole-body distribution & depuration of nanoplastics by
648 the scallop *Pecten maximus*, at environmentally realistic concentrations. *Environ. Sci.*
649 *Technol.* **52**, 14480–14486 (2018).
- 650 11. Skjolding, L. M. *et al.* An assessment of the importance of exposure routes to the uptake and
651 internal localisation of fluorescent nanoparticles in zebrafish (*Danio rerio*), using light sheet
652 microscopy. *Nanotoxicology* **11(3)**, 351–359 (2017).
- 653 12. Brun, N. R. *et al.* Polystyrene nanoplastics disrupt glucose metabolism and cortisol levels
654 with a possible link to behavioural changes in larval zebrafish. *Commun. Biol.* **2**, (2019).
- 655 13. Li, J., Liu, H. & Paul Chen, J. Microplastics in freshwater systems: A review on occurrence,
656 environmental effects, and methods for microplastics detection. *Water Res.* **137**, 362–374
657 (2018).
- 658 14. Tournier, V. *et al.* An engineered PET depolymerase to break down and recycle plastic
659 bottles. *Nature* **580**, 216–219 (2020).
- 660 15. Fu, W., Min, J., Jiang, W., Li, Y. & Zhang, W. Separation, characterization and identification
661 of microplastics and nanoplastics in the environment. *Sci. Total Environ.* **721**, 137561
662 (2020).
- 663 16. Schwaferts, C., Niessner, R., Elsner, M. & Ivleva, N. P. Methods for the analysis of
664 submicrometer- and nanoplastic particles in the environment. *TrAC - Trends in Analytical*
665 *Chemistry* vol. 112 52–65 (2019).
- 666 17. Wang, L. *et al.* Environmental fate, toxicity and risk management strategies of nanoplastics
667 in the environment: Current status and future perspectives. *J. Hazard. Mater.* **401**, (2021).
- 668 18. Coppock, R. L., Cole, M., Lindeque, P. K., Queirós, A. M. & Galloway, T. S. A small-scale,
669 portable method for extracting microplastics from marine sediments. *Environ. Pollut.* **230**,

- 670 829–837 (2017).
- 671 19. Kedzierski, M. *et al.* Microplastics elutriation from sandy sediments: A granulometric
672 approach. *Mar. Pollut. Bull.* **107**, 315–323 (2016).
- 673 20. Rocha-Santos, T. & Duarte, A. C. A critical overview of the analytical approaches to the
674 occurrence, the fate and the behavior of microplastics in the environment. *TrAC - Trends*
675 *Anal. Chem.* **65**, 47–53 (2015).
- 676 21. Kontturi, E. *et al.* Advanced Materials through Assembly of Nanocelluloses. *Adv. Mater.* **30**,
677 (2018).
- 678 22. Jafari, S. *et al.* Recovery of gold from chloride solution by TEMPO-oxidized cellulose
679 nanofiber adsorbent. *Sustain.* **11**, (2019).
- 680 23. Hakalahti, M., Faustini, M., Boissière, C., Kontturi, E. & Tammelin, T. Interfacial
681 Mechanisms of Water Vapor Sorption into Cellulose Nanofibril Films as Revealed by
682 Quantitative Models. *Biomacromolecules* **18**, 2951–2958 (2017).
- 683 24. Kangas, H. *et al.* Characterization of fibrillated celluloses. A short review and evaluation of
684 characteristics with a combination of methods. *Nord. Pulp Pap. Res. J.* (2014)
685 doi:10.3183/npprj-2014-29-01-p129-143.
- 686 25. Flauraud, V. *et al.* Nanoscale topographical control of capillary assembly of nanoparticles.
687 *Nat. Nanotechnol.* **12**, 73–80 (2017).
- 688 26. Saito, T., Nishiyama, Y., Putaux, J. L., Vignon, M. & Isogai, A. Homogeneous suspensions
689 of individualized microfibrils from TEMPO-catalyzed oxidation of native cellulose.
690 *Biomacromolecules* **7**, 1687–1691 (2006).
- 691 27. Fernandes Diniz, J. M. B., Gil, M. H. & Castro, J. a a M. Hornification - Its origin and
692 interpretation in wood pulps. *Wood Sci. Technol.* **37**, 489–494 (2004).

- 693 28. Walker, D. A., Kowalczyk, B., De, O. & Grzybowski, B. A. Nanoscale Electrostatics at the
694 nanoscale. 1316–1344 (2011) doi:10.1039/c0nr00698j.
- 695 29. Sanchez-Vidal, A., Canals, M., de Haan, W. P., Romero, J. & Veny, M. Seagrasses provide a
696 novel ecosystem service by trapping marine plastics. *Sci. Rep.* **11**, 254 (2021).
- 697 30. Tarjus, G., Schaaf, P. & Talbot, J. Generalized random sequential adsorption. *J. Chem. Phys.*
698 **93**, (1990).
- 699 31. Schaaf, P. & Talbot, J. Kinetics of Random Sequential Adsorption. *Phys. Rev. Lett.* **62**(2),
700 175–178 (1989).
- 701 32. Hemmersam, A. G., Rechendorff, K., Foss, M., Sutherland, D. S. & Besenbacher, F.
702 Fibronectin adsorption on gold, Ti-, and Ta-oxide investigated by QCM-D and RSA
703 modelling. *J. Colloid Interface Sci.* **320**, 110–116 (2008).
- 704 33. Reimhult, E., Larsson, C., Kasemo, B. & Höök, F. Simultaneous surface plasmon resonance
705 and quartz crystal microbalance with dissipation monitoring measurements of biomolecular
706 adsorption events involving structural transformations and variations in coupled water. *Anal.*
707 *Chem.* **76**, 7211–7220 (2004).
- 708 34. Johansson, L. S., Tammelin, T., Campbell, J. M., Setälä, H. & Österberg, M. Experimental
709 evidence on medium driven cellulose surface adaptation demonstrated using nanofibrillated
710 cellulose. *Soft Matter* **7**, 10917–10924 (2011).
- 711 35. Yamane, C. *et al.* Two different surface properties of regenerated cellulose due to structural
712 anisotropy. *Polym. J.* **38**, 819–826 (2006).
- 713 36. Suchy, M., Virtanen, J., Kontturi, E. & Vuorinen, T. Impact of drying on wood ultrastructure
714 observed by deuterium exchange and photoacoustic FT-IR spectroscopy. *Biomacromolecules*
715 **11**, 515–520 (2010).

- 716 37. Heise, K. *et al.* Nanocellulose: Recent Fundamental Advances and Emerging Biological and
717 Biomimicking Applications. *Adv. Mater.* **33**, 2004349 (2021).
- 718 38. Osmekhina, E. *et al.* Controlled communication between physically separated bacterial
719 populations in a microfluidic device. *Commun. Biol.* **1**, (2018).
- 720 39. Xia, Y. & Whitesides, G. M. SOFT LITHOGRAPHY. *Annu. Rev. Mater. Sci.* (1998)
721 doi:10.1146/annurev.matsci.28.1.153.
- 722 40. Osmekhina, E., Shvetsova, A., Ruottinen, M. & Neubauer, P. Quantitative and sensitive
723 RNA based detection of Bacillus spores. *Front. Microbiol.* (2014)
724 doi:10.3389/fmicb.2014.00092.
- 725 41. Hakalahti, M., Salminen, A., Seppälä, J., Tammelin, T. & Hänninen, T. Effect of interfibrillar
726 PVA bridging on water stability and mechanical properties of TEMPO/NaClO₂ oxidized
727 cellulosic nanofibril films. *Carbohydr. Polym.* **126**, 78–82 (2015).
- 728 42. Ahola, S., Salmi, J., Johansson, L.-S., Laine, J. & Österberg, M. Model Films from Native
729 Cellulose Nanofibrils. Preparation, Swelling, and Surface Interactions. *Biomacromolecules* **9**,
730 1273–1282 (2008).
- 731 43. Kontturi, E., Thü Ne, P. C. & Niemantsverdriet, H. Cellulose Model Surfaces Simplified
732 Preparation by Spin Coating and Characterization by X-ray Photoelectron Spectroscopy,
733 Infrared Spectroscopy, and Atomic Force Microscopy. (2003) doi:10.1021/la0340394.
- 734 44. Reviakine, I., Johannsmann, D. & Richter, R. P. Hearing what you cannot see and visualizing
735 what you hear: Interpreting quartz crystal microbalance data from solvated interfaces. *Anal.*
736 *Chem.* **83**, 8838–8848 (2011).
- 737 45. Sauerbrey, G. Z. Use of quartz vibration for weighing thin films on a microbalance. *Phys. J*
738 (1959).

- 739 46. Miles, R. On the elimination of edge-effects in planar sampling. in *Stochastic geometry* (eds.
740 Harding, E. & Kendall, D.) 228–247 (John Wiley and Sons, Inc., 1972).
- 741 47. Lavalle, P., Schaaf, P., Ostafin, M., Voegel, J.-C. & Senger, B. Extended random sequential
742 adsorption model of irreversible deposition processes: From simulations to experiments.
743 *Proc. Natl. Acad. Sci.* **96**, 11100–11105 (1999).
- 744 48. Min, H. *et al.* Modified Random Sequential Adsorption Model for Understanding Kinetics of
745 Proteins Adsorption at a Liquid-Solid Interface. *Langmuir* **33**, 7215–7224 (2017).
- 746 49. Schaaf, P. & Talbot, J. Surface exclusion effects in adsorption processes. *J. Chem. Phys.* **91**,
747 4401–4409 (1989).
- 748 50. Manzi, B. M., Werner, M., Ivanova, E. P., Crawford, R. J. & Baulin, V. A. Simulations of
749 Protein Adsorption on Nanostructured Surfaces. *Sci. Rep.* **9**, (2019).
- 750

Figures

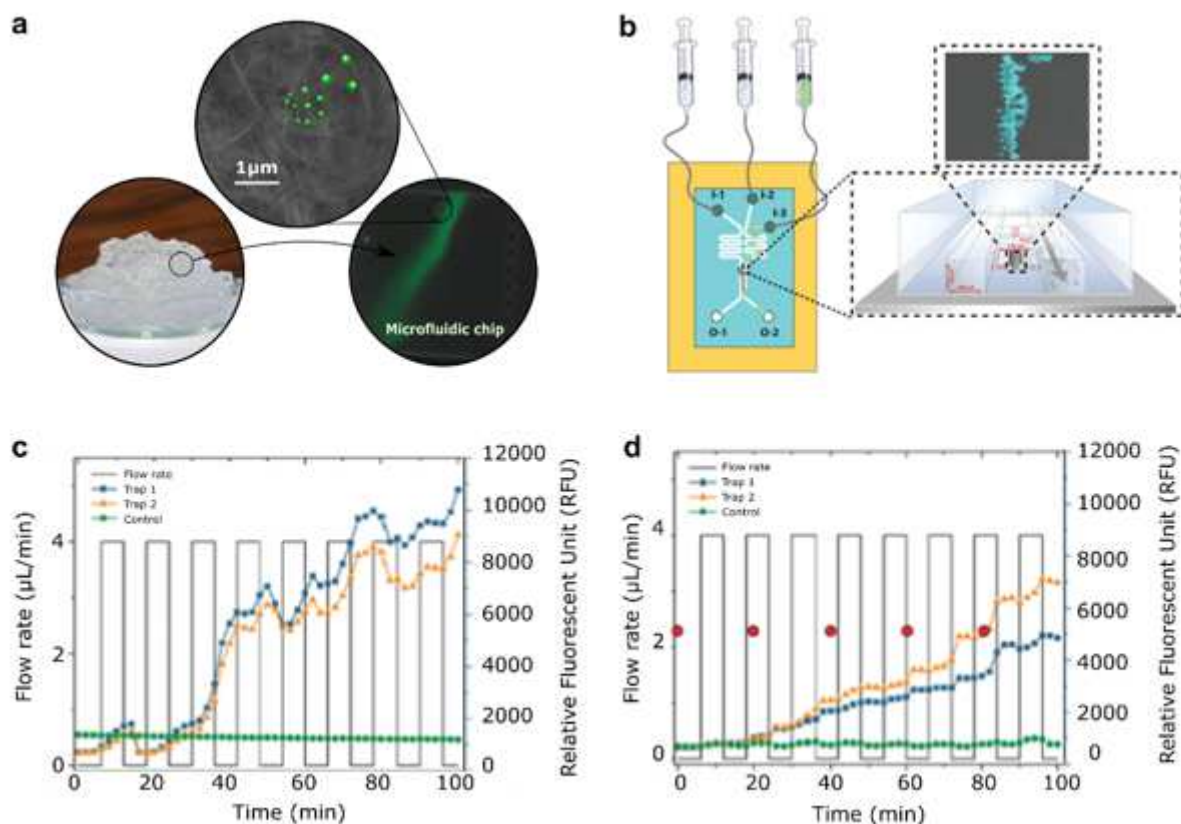


Figure 1

Capture of microplastic particles by native CNF hydrogel network. a, Schematic illustration of a proof of concept where the capture of fluorescently labelled microplastic particles by CNF hydrogel network is verified using a microfluidic set-up and fluorescent imaging (Extended Data Video 1). b. Schematic illustrations of the microfluidic setup for CNF containing trap showing the injection of fluorescent nPp and μ Pp (I-3) and water (I-2/I-1). I-1 channel is used to pack the CNF hydrogel into the connected traps and I-2 is used for washing. Fluorescent accumulation of nPp (c) and μ Pp (d) over time by CNF hydrogel network. Green curves show control trap without CNF hydrogel. The orange and blue curves show parallel experiments with CNF in the traps. In d, the red dots indicate the time points where microscopy images were taken (Supplementary Fig. 1).

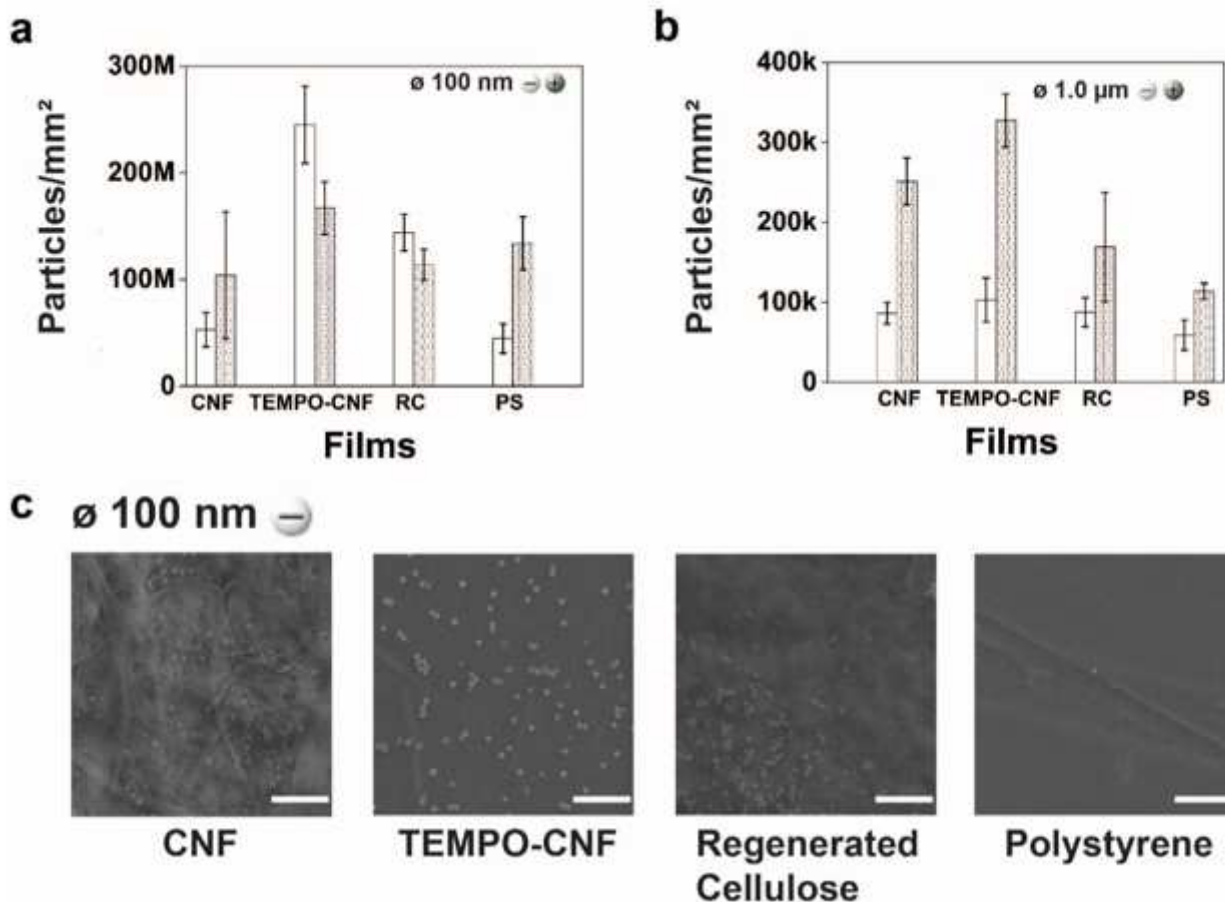


Figure 2

Quantitative assessment of entrapped fluorescent microplastic particles of different size and charge by self-standing films. a, Number of captured nPp and b, μ Pp calculated based on the fluorescence detection. White bars represent negatively charged plastic particles, and grey bars positively charged plastic particles. The full data for all captured particles is presented in Supplementary Table 2. c, SEM images of the films after being contacted with the aqueous nPp dispersion for 10 min. Scale bar in SEM images is 1 μ m.

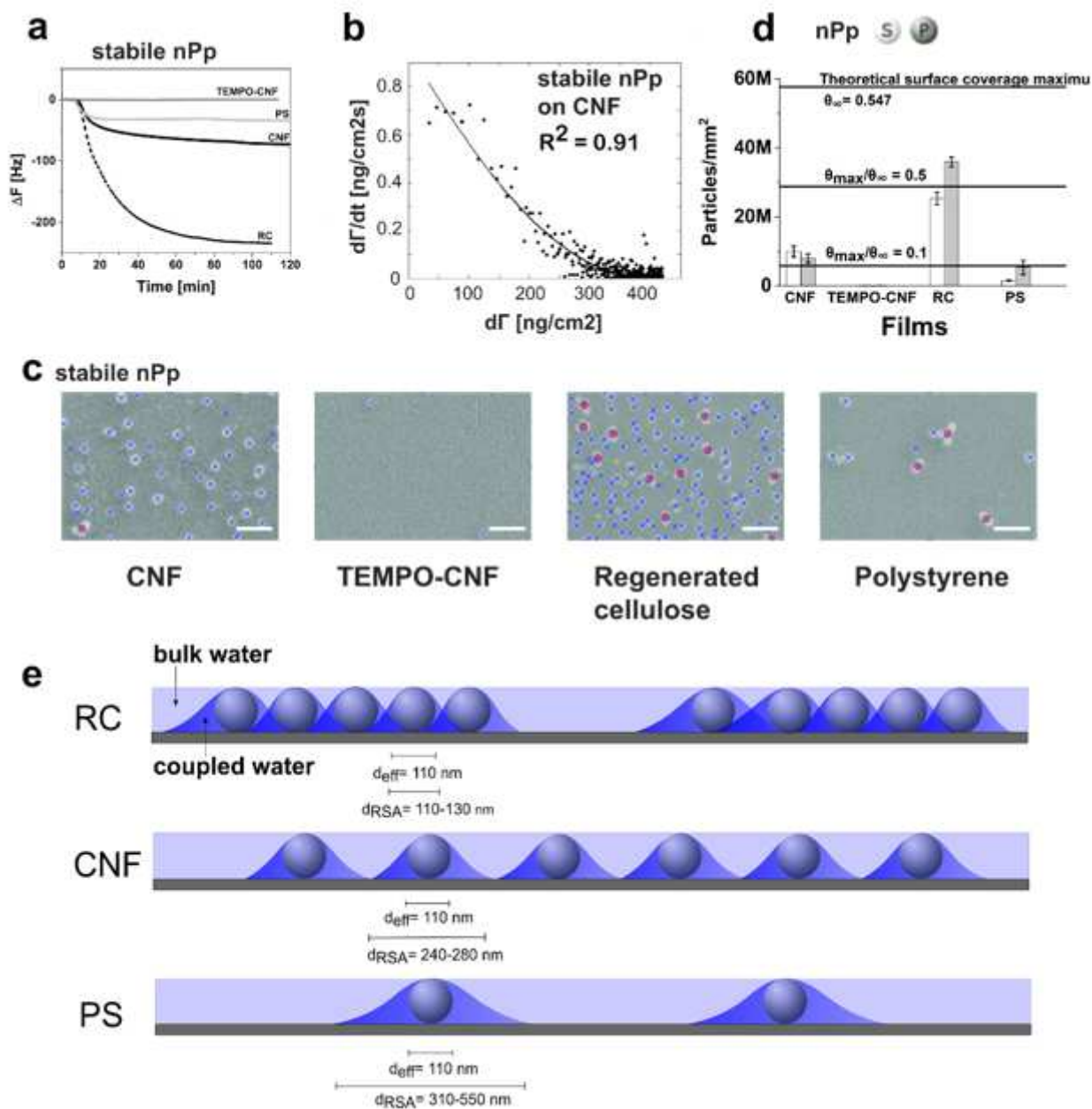


Figure 3

Quantitative assessment of surface binding of nPp using surface sensitive approach coupled with image analysis and fittings with random sequential adsorption (RSA) model. a, QCM-D frequency change responses showing the adsorption of stabile nPp on TEMPO-CNF (dark gray line), PS (grey line), native CNF (solid black line), and RC (dashed black line). b, Fitting of the QCM-D adsorption data of stabile nPp on CNF using the RSA model. Black dots are measured data, and black line is the RSA fit. The adjusted R2 for the fit is 0.91. c, Stabile nPp recognition from scanning electron microscopy (SEM) images using image analysis (Supplementary Fig 9). The SEM image scale bar is 0.5 μm . d, Amount of nPp detected after the adsorption experiments (white bars stabile, grey bars purified) via image analysis of SEM micrographs contrasted to a theoretical surface coverage maximum ($\theta_\infty = 0.547$ which equals to $\sim 5.8 \times 10^{-7}$ circles mm^2), which is based on the RSA model. e, Schematic presentations display the appearance

of substrates at the end of the nPp adsorption process showing the existence of bulk water and water which is strongly interacting with nPp. d_{eff} describes the effective particle diameter, and d_{RSA} is the diameter of the occupied area (a) of a single nPp including the particle and the coupled water.

Supplementary Files

This is a list of supplementary files associated with this preprint. Click to download.

- [LeppXXnenetalExtendedDataVideo1.mp4](#)
- [LeppXXnenetalNatureCommunicationsSupplementary2021.docx](#)